UNIVERSITY OF CALIFORNIA SAN DIEGO

Aerodynamics of Tsuji Burners with Augmented Fuel Injection

A thesis submitted in partial satisfaction of the
requirements for the degree
Master of Science

in

Engineering Sciences (Aerospace Engineering)

by

Brandon Li

Committee in charge:

Professor Antonio Sanchez, Chair
Professor Abhishek Saha
Professor Forman Williams

2021

The thesis of Brandon Li is approved, and it is acceptable in quality and form for publication on microfilm and electronically.

University of California San Diego

2021

DEDICATION

To researchers for their efforts to create a better understanding of mathematics and the world we live in.

EPIGRAPH

Humanity's deepest desire for knowledge is justification enough for our continuing quest. And our goal is nothing less than a complete description of the universe we live in.

—Stephen Hawking

TABLE OF CONTENTS

LIST OF FIGURES

ACKNOWLEDGEMENTS

I would like to thank Dr. José Graña Otero for all of his help on this project. He has introduced me to many new topics on numerical methods and spent a lot of time guiding me through various approaches used to solve our problem. He has also helped tremendously with the writeup.

I am also grateful for my advisor, Professor Antonio Sánchez for giving me the opportunity to work with him on this project. I have learned and grown as a student so much this year, and a lot of it is due to his guidance and support.

I would also like to thank my family and friends for supporting my decision to enter graduate school. Their encouragement gave me confidence and the desire to succeed. I am especially grateful for my parents, who were very understanding of me and supported me at all levels.

Last but not least, I would like to thank my girlfriend, Ashley Ge, for her support. Whenever there were difficult times - academically related or not - she would always be there.

Material from this thesis is currently being prepared for publication in Combustion Science and Technology and Combustion and Flame. This thesis is coauthored with Sánchez, Antonio; Graña, José; and Williams, Forman. The thesis author is the primary author of this material.

VITA

2020	B. S. in Aerospace Engineering cum laude, University of California San Diego
2021	Graduate Teaching Assistant, University of California San Diego
2021	M. S. in Aerospace Engineering, University of California San Diego

ABSTRACT OF THE THESIS

Aerodynamics of Tsuji Burners with Augmented Fuel Injection

by

Brandon Li

Master of Science in Engineering Sciences (Aerospace Engineering)

University of California San Diego 2021

Professor Antonio Sanchez, Chair

This thesis addresses the aerodynamics of Tsuji burners, involving a flame developing from the forward stagnation region of a cylindrical porous fuel injector placed in an air stream. Attention is focused on cases when the fuel-injection velocity is comparable to the outer air velocity, so that the boundary layer is blown off from the cylinder surface. In the resulting flow, the flame is embedded in the thin mixing layer that forms about the stream surface separating the outer air stream from the fuel stream, both having in general different density. The flow structure, nearly inviscid outside the mixing layer, is investigated here for cases where the porous fuel injector is placed in a uniform air stream or at the center of a symmetrical planar counterflow configuration. In both cases the velocity on the air side of

the mixing layer is potential, while the velocity found on the fuel side is rotational, because fuel injection generates vorticity through the requirement that fuel emerges normal to the cylinder surface. It is shown that introduction of a density-weighted streamfunction reduces the problem to the case of constant-density flow, with the density-square-root-weighted ratio of injection velocity to free-stream velocity Λ emerging as the only controlling parameter. The numerical solution, involving the determination of the vorticity distribution through an iterative scheme, provides the structure of the flow, including the location of the flame and associated strain-rate distribution. Numerical results are presented for values of Λ ranging from small injection velocities $\Lambda \ll 1$ to large injection velocities $\Lambda \gg 1$. The inviscid results reported here in the limit of vanishingly small injection velocities $\Lambda \ll 1$ indicate that the outer air velocity never approaches the classical solution corresponding to potential flow with $\Lambda = 0$, a result with important implications for the analysis of flames stabilized in Tsuji burners.

Chapter 1

Introduction

Tsuji burners have been used to investigate laminar counterflow flames for over 50 years [1]. As indicated in the schematic shown on the left-hand side of Fig. 1.1, the flame is established in the forward stagnation-point region of a porous cylinder of radius a placed in a uniform air stream of velocity U_∞, with the fuel released by injection perpendicular to the cylinder surface with velocity U_i. In most applications, the Reynolds number $Re = \rho_A U_\infty a/\mu_A$ (based on the density ρ_A and viscosity μ_A of the air stream) is large and the injection velocity U_i is small, of order $U_i \sim U_\infty/Re^{1/2}$, so that the streamline separating the external air flow from the fuel flow lies in the near-wall boundary layer of characteristic thickness $\delta = a/Re^{1/2} \ll a$ that develops over the forward side of the cylinder. Effects of molecular transport are confined to this boundary layer, where the fuel and the air mix and react, while the flow outside is nearly inviscid, with an azimuthal velocity component on the outer edge of the boundary layer that can be approximated near the forward stagnation point by the potential flow solution. In this forward stagnation region the solution in the reacting boundary layer is selfsimilar [2], determined by the value of the local strain rate (i.e. $2U_\infty/a$, according to the potential solution). The reacting boundary layer, containing the flame, continues developing along the cylinder wall away from the stagnation region,

until separation eventually occurs.

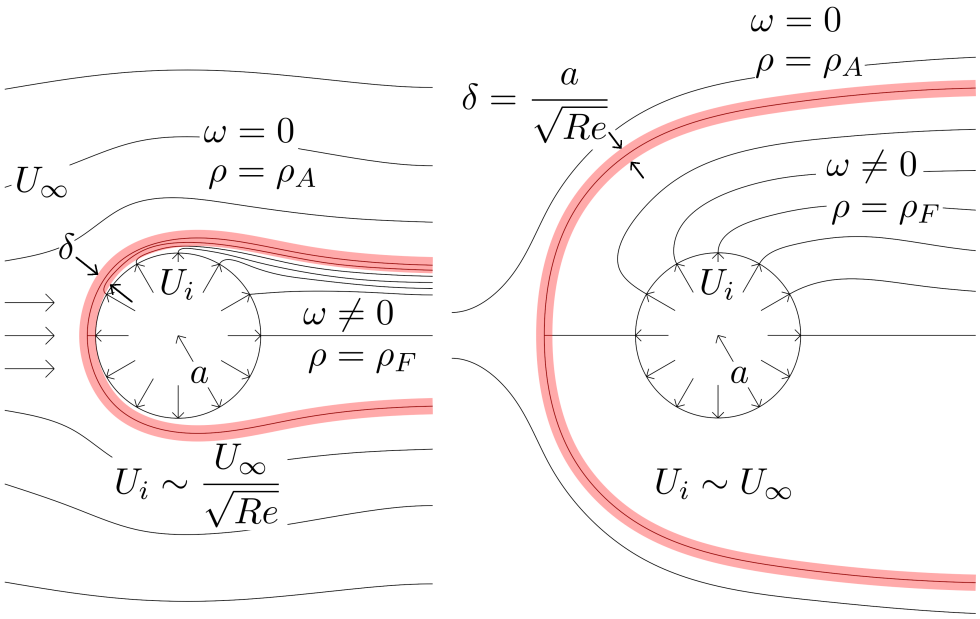

Figure 1.1: A schematic view of the flow field in Tsuji burners with $U_i \sim U_\infty/Re^{1/2}$ (left plot) and with $U_i \sim U_\infty$ (right plot).

The flow structure depicted on the left-hand side of Fig. 1.1, corresponding to injection velocities $U_i \sim U_\infty/Re^{1/2} \ll U_\infty$, changes drastically when the fuel is injected with velocities that are comparable to U_∞, displacing the stagnation point at distances of order a away from the cylinder surface, as shown on the right-hand side of Fig. 1.1. For $Re \gg 1$, mixing and reaction occur only in a thin mixing layer of characteristic thickness $\delta = a/Re^{1/2} \ll a$ localized at the fluid interface separating the incoming air flow from the injected fuel gas. At leading order in the limit $Re \gg 1$ the reacting mixing layer emerges as a free surface $r_s(\theta)$ separating two regions of inviscid flow, as indicated in Fig. 1.1. The outer flow is potential, because the air stream carries no vorticity, but the inner flow is rotational, because the injected fuel stream has vorticity, as needed for the injection velocity to be normal to the cylinder surface. Besides the classical Tsuji burner, consideration will be given to the case of a porous cylinder placed at the center of a planar counterflow with strain rate A_∞, a configuration that has been recently proposed for studying transition

from counterflow to coflow flames [3]. The two configurations investigated here are shown in Fig. 1.2.

We begin below by formulating the problem for general order-unity values of the Reynolds number $Re = \rho_A U_c a/\mu_A$ based on the characteristic air velocity $U_c = U_\infty$ or $U_c = A_\infty a$. Consideration of the limit $Re \gg 1$ will be seen to reduce the problem to that of inviscid flow, with the solution depending in general on two parameters, namely, the fuel-to-air density ratio ρ_F/ρ_A and the fuel-to-air velocity ratio U_i/U_c. Use of a density-weighted vorticity-streamfunction formulation [4, 5] further reduces the problem to the constant-density case, with $\Lambda = (\rho_F/\rho_A)^{1/2} U_i/U_c$ entering as the only governing parameter. The solution involves the determination of the vorticity distribution on the cylinder surface, which will be computed numerically for different values of Λ. The solution provides the location of the forward stagnation point and the associated local value of the strain rate. The shape of the streamline separating the two reactant streams and the streamwise variation of the velocity will also be obtained.

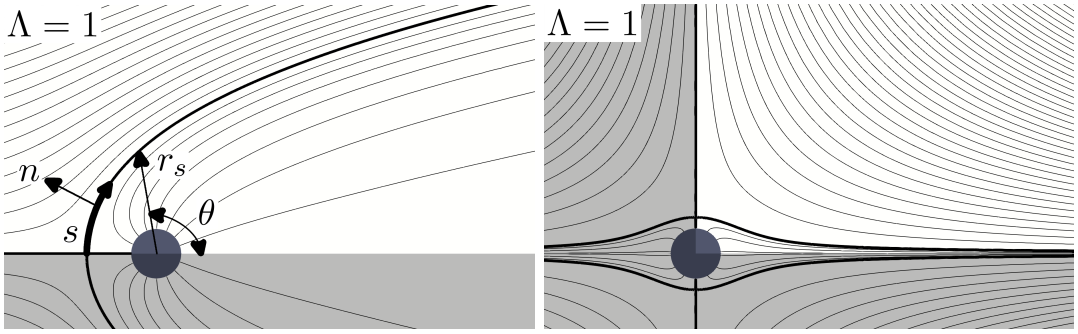

Figure 1.2: The two flow configurations investigated here. For both, the streamlines shown correspond to the case $\Lambda = 1$.

Chapter 2

Formulation of the problem

The two porous-burner configurations investigated here are shown in Fig. 1.2. The cylinder radius a and characteristic velocity U_c ($U_c = U_\infty$ for the uniform-flow configuration and $U_c = A_\infty a$ for the counterflow configuration) will be used to scale the problem, yielding dimensionless cylindrical coordinates (r, θ) and corresponding velocity $\mathbf{v} = (v_r, v_\theta)$. Following standard convention, the azimuthal angle θ is to be measured counterclockwise from the horizontal rightward ray, with the uniform air flow approaching from $\theta = \pi$ and the counterflow air streams approaching from $\theta = \pm\pi/2$. Because of the existing symmetry, it suffices to give the solution in either the half plane $0 \leq \theta \leq \pi$ (for uniform flow) or in the first quadrant $0 \leq \theta \leq \pi/2$ (for the counterflow).

The air density ρ_A and temperature T_A will be used to define a dimensionless density ρ and a dimensionless temperature T. Similarly, the transport properties of the air stream will be used to define a dimensionless viscosity μ, heat conductivity k, and molecular diffusivity D_i of species i. Buoyancy forces are neglected in the analysis, an appropriate simplification for small combustors with sufficiently large Froude numbers $U_c^2/(ga) \gg 1$. For the low-Mach-number conditions prevailing in applications, the steady form of the conservation equations [6] for a reacting gas mixture with constant specific heat c_p reduce

to

$$\begin{aligned}
\nabla \cdot (\rho \mathbf{v}) &= 0 && (2.1)\\
\rho \mathbf{v} \cdot \nabla \mathbf{v} &= -\nabla p + \frac{1}{Re} \nabla \cdot [\mu (\nabla \mathbf{v} + \nabla \mathbf{v}^T)] && (2.2)\\
\rho \mathbf{v} \cdot \nabla T &= \frac{1}{Pr Re} \nabla \cdot (k \nabla T) - \sum_N \frac{\dot{m}_i}{(\rho_A U_c / a)} \frac{h_i}{(c_p T_A)}, && (2.3)\\
\rho \mathbf{v} \cdot \nabla Y_i &= \frac{1}{Sc_i Re} \nabla \cdot (\rho D_i \nabla Y_i) + \frac{\dot{m}_i}{\rho_A U_c / a}, && (2.4)
\end{aligned}$$

where p represents the spatial pressure differences scaled with $\rho_A U_c^2$, Pr is the Prandtl number and Y_i, h_i, and Sc_i denote the mass fraction, enthalpy of formation, and Schmidt number of species i. The production rate $\dot{m}_i$ of chemical species i, identically zero in the feed streams, must be evaluated for a given chemistry description in terms of the local values of T and Y_i. The above equations must be supplemented with expressions for the temperature and composition dependences of the dimensionless transport coefficients k, μ, and D_i and with the equation of state written in the low-Mach-number form

$$\rho T \sum_i (Y_i W_A / W_i) = 1, \tag{2.5}$$

with W_i and W_A denoting, respectively, the molecular mass of species i and the mean molecular mass of the air stream. In integrating the problem one needs to specify the temperature and composition of the air stream as $r \to \infty$ and of the fuel stream at $r = 1$, with corresponding boundary velocity distributions given by

$$\begin{cases} (v_r, v_\theta) \to (\cos\theta, \sin\theta) & \text{(uniform flow)} \\ (v_r, v_\theta) \to r[\cos(2\theta), -\sin(2\theta)] & \text{(counterflow)} \end{cases} \tag{2.6}$$

as $r \to \infty$ and

$$v_r - U_i / U_c = v_\theta = 0 \tag{2.7}$$

at $r = 1$.

2.1 The limit $\boldsymbol{Re} \gg 1$

In the inviscid limit $Re \gg 1$ molecular transport becomes negligible in (2.2)–(2.4). In the absence of mixing, the chemical reaction cannot proceed, so that (2.3) and (2.4) reduce to $\mathbf{v} \cdot \nabla T = \mathbf{v} \cdot \nabla Y_i = 0$, indicating that the temperature and composition of the steady flow, and therefore also the density according to (2.5), remain constant along streamlines. As a result, there exists a fluid interface $r = r_s(\theta)$ separating an external region with density $\rho = 1$ from an internal region with density $\rho = \rho_F/\rho_A$. This separating interface $r = r_s(\theta)$ is a tangential discontinuity, with the velocity on the outer and inner sides satisfying

$$|\mathbf{v}^+|^2 = (\rho_F/\rho_A)|\mathbf{v}^-|^2, \tag{2.8}$$

as follows from conservation of head along the boundary streamlines, with the superscripts $+$ and $-$ denoting conditions at $r = r_s^+$ and $r = r_s^-$, respectively.

The problem can be conveniently formulated in terms of the streamfunction ψ, defined such that

$$v_r = \frac{1}{r}\frac{\partial \psi}{\partial \theta} \quad \text{and} \quad v_\theta = -\frac{\partial \psi}{\partial r}. \tag{2.9}$$

For the planar flow investigated here, the vorticity

$$\omega = \frac{1}{r}\frac{\partial}{\partial r}(r v_\theta) - \frac{1}{r^2}\frac{\partial v_r}{\partial \theta} \tag{2.10}$$

satisfies

$$v_r \frac{\partial \omega}{\partial r} + \frac{v_\theta}{r}\frac{\partial \omega}{\partial \theta} = 0, \tag{2.11}$$

as can be seen by taking the curl of the inviscid form of (2.2). Equation (2.11) reveals

that the vorticity is conserved along streamlines, so that $\omega = \omega(\psi)$. Using (2.9) in (2.10) provides

$$\frac{1}{r}\frac{\partial}{\partial r}\left(r\frac{\partial \psi}{\partial r}\right) + \frac{1}{r^2}\frac{\partial^2 \psi}{\partial \theta^2} = -\omega(\psi), \tag{2.12}$$

as an equation for ψ in terms of the unknown function $\omega(\psi)$. The boundary conditions needed for integrating (2.12) are different for the two flow configurations depicted in Fig. 1.2. For example, for the uniform air-flow configuration the streamfunction satisfies

$$\begin{cases} \psi - (U_i/U_\infty)\,(\theta - \pi) = \partial\psi/\partial r = 0 & \text{at } r = 1 \quad \text{for } 0 \le \theta \le \pi \\ \psi = 0 & \text{at } \theta = \pi \quad \text{for } 1 \le r < \infty \\ \psi \to r\sin\theta & \text{as } r \to \infty \quad \text{for } 0 < \theta \le \pi \\ \psi = -\pi(U_i/U_\infty) & \text{at } \theta = 0 \quad \text{for } 1 \le r < \infty \end{cases} \tag{2.13}$$

when account is taken of the symmetry present in the problem. The arbitrary value of ψ along $r = r_s(\theta)$ is selected to be $\psi = 0$, with the air/fuel sides corresponding to positive/negative values of ψ, respectively. The separating surface $r = r_s(\theta)$ is an unknown free boundary to be determined with use made of the additional boundary condition (2.8) written in the form

$$\left[\left(\frac{\partial \psi}{\partial r}\right)^2 + \frac{1}{r^2}\left(\frac{\partial \psi}{\partial \theta}\right)^2\right]^+ = \left(\frac{\rho_F}{\rho_A}\right)\left[\left(\frac{\partial \psi}{\partial r}\right)^2 + \frac{1}{r^2}\left(\frac{\partial \psi}{\partial \theta}\right)^2\right]^- \quad \text{at} \quad \psi = 0. \tag{2.14}$$

The function $\omega(\psi)$ is related to the unknown distribution of vorticity on the cylinder wall $\omega_w(\theta)$ through

$$\omega = \begin{cases} 0 \quad \text{for } \psi \ge 0 \\ \omega_w[(U_\infty/U_i)\psi + \pi] \quad \text{for } -\pi(U_i/U_\infty) \le \psi \le 0 \end{cases}. \tag{2.15}$$

2.2 Reduction to the case of equal densities

The free-boundary problem defined in (2.12)–(2.15) determines $\psi(r,\theta)$ along with the vorticity distribution $\omega_w(\theta)$ and the separating surface $r_s(\theta)$ for given values of U_i/U_∞ and ρ_F/ρ_A. As shown in [4, 5], the solution can be simplified by incorporating a renormalization factor $(\rho_F/\rho_A)^{1/2}$ in the definition of new kinematic variables

$$\hat{\omega} = (\rho_F/\rho_A)^{1/2}\omega \quad \text{and} \quad \hat{\psi} = \begin{cases} \psi & \text{for } \psi > 0 \\ (\rho_F/\rho_A)^{1/2}\psi & \text{for } \psi < 0 \end{cases} . \tag{2.16}$$

The conservation equation for the streamfunction becomes

$$\frac{1}{r}\frac{\partial}{\partial r}\left(r\frac{\partial\hat{\psi}}{\partial r}\right) + \frac{1}{r^2}\frac{\partial^2\hat{\psi}}{\partial\theta^2} = -\hat{\omega}(\hat{\psi}). \tag{2.17}$$

For the case of uniform air flow (left-hand side of Fig. 1.2) the boundary conditions are

$$\begin{cases} \hat{\psi} - \Lambda\,(\theta-\pi) = \partial\hat{\psi}/\partial r = 0 & \text{at } r = 1 & \text{for } 0 \le \theta \le \pi \\ \hat{\psi} = 0 & \text{at } \theta = \pi & \text{for } 1 \le r < \infty \\ \hat{\psi} \to r\sin\theta & \text{as } r \to \infty & \text{for } 0 < \theta \le \pi \\ \hat{\psi} = -\pi\Lambda & \text{at } \theta = 0 & \text{for } 1 \le r < \infty \end{cases} \tag{2.18}$$

and the relation between the rescaled vorticity and its distribution on the cylinder surface $\hat{\omega}_w(\theta)$ is

$$\hat{\omega} = \begin{cases} 0 \quad \text{for } \hat{\psi} \ge 0 \\ \hat{\omega}_w(\psi/\Lambda + \pi) \quad \text{for } -\pi\Lambda \le \hat{\psi} \le 0 \end{cases} . \tag{2.19}$$

On the other hand, for the case of an external counterflow (right-hand side of Fig. 1.2) the boundary conditions are

$$\begin{cases} \hat{\psi} - \Lambda\,(\theta - \pi/2) = \partial\hat{\psi}/\partial r = 0 & \text{at } r = 1 & \text{for } 0 \le \theta \le \pi/2 \\ \hat{\psi} = 0 & \text{at } \theta = \pi/2 & \text{for } 1 \le r < \infty \\ \hat{\psi} \to (r^2/2)\sin(2\theta) & \text{as } r \to \infty & \text{for } 0 < \theta \le \pi/2 \\ \hat{\psi} = -(\pi/2)\Lambda & \text{at } \theta = 0 & \text{for } 1 \le r < \infty \end{cases} \tag{2.20}$$

and the rescaled vorticity satisfies

$$\hat{\omega} = \begin{cases} 0 \quad \text{for } \hat{\psi} \ge 0 \\ \hat{\omega}_w(\psi/\Lambda + \pi/2) \quad \text{for } -\pi\Lambda/2 \le \hat{\psi} \le 0 \end{cases} . \tag{2.21}$$

The dynamic condition (2.14) is automatically satisfied, thereby removing the need to consider the separating surface $r_s(\theta)$ as a free boundary. As can be seen, the reduced formulation depends on the single governing parameter Λ, defined as

$$\Lambda = \left(\frac{\rho_F}{\rho_A}\right)^{1/2} \frac{U_i}{U_\infty} \tag{2.22}$$

in (2.18) and

$$\Lambda = \left(\frac{\rho_F}{\rho_A}\right)^{1/2} \frac{U_i}{A_\infty a} \tag{2.23}$$

in (2.20). The solutions depicted in Fig. 1.2 correspond to $\Lambda = 1$.

The solution to the above problem determines $\hat{\psi}(r, \theta)$ as well as the vorticity distribution on the cylinder surface $\hat{\omega}_w(\theta)$. The latter is ultimately determined by the condition that the fuel is injected perpendicular to the wall, in that there is a single distribution $\hat{\omega}_w(\theta)$ for which $\partial\hat{\psi}/\partial r = 0$ at $r = 1$. For example, if the fuel were injected

with zero vorticity, then the stream function would be given by the potential-flow solution

$$\begin{cases} \hat{\psi}_p = (r - 1/r)\sin\theta + \Lambda(\theta - \pi) & \text{(uniform flow)} \\ \hat{\psi}_p = (r^2 - 1/r^2)\sin(2\theta)/2 + \Lambda(\theta - \pi/2) & \text{(counterflow)} \end{cases} \tag{2.24}$$

with corresponding nonzero values $\partial\hat{\psi}/\partial r = 2\sin\theta$ (uniform flow) and $\partial\hat{\psi}/\partial r = 2\sin(2\theta)$ (counterflow) at $r = 1$. It is worth noting that the potential solution given in the second equation of (2.24) has been reasoned to be sufficiently accurate for the analysis of porous burners in the counterflow configuration [3]. The predictive capability of this description, which neglects the presence of vorticity on the fuel side of the flame, is to be assessed through comparison with our numerical results.

Chapter 3

The numerical scheme

The computation of $\hat{\omega}_w(\theta)$ emerges as a complicating characteristic in the numerical integration that warrants specific attention, as explained below. To facilitate the solution, it is convenient to express the stream function in the form $\hat{\psi} = \hat{\psi}_p + \hat{\psi}_r$, where ψ_p is the potential distribution given by (2.24) and $\hat{\psi}_r$ is the rotational component, the latter determined by integration of

$$\frac{1}{r}\frac{\partial}{\partial r}\left(r\frac{\partial\hat{\psi}_r}{\partial r}\right) + \frac{1}{r^2}\frac{\partial^2\hat{\psi}_r}{\partial\theta^2} = -\hat{\omega}(\hat{\psi}_p + \hat{\psi}_r). \tag{3.1}$$

with boundary conditions

$$\begin{cases} \hat{\psi}_r = \partial\hat{\psi}_r/\partial r + 2\sin\theta = 0 & \text{at } r = 1 \quad \text{for } 0 \le \theta \le \pi \\ \hat{\psi}_r = 0 & \text{at } \theta = \pi \quad \text{for } 1 \le r < \infty \\ \hat{\psi}_r \to 0 & \text{as } r \to \infty \quad \text{for } 0 \le \theta \le \pi \\ \hat{\psi}_r = 0 & \text{at } \theta = 0 \quad \text{for } 1 \le r < \infty \end{cases} \tag{3.2}$$

for uniform external flow and

$$\begin{cases} \hat{\psi}_r = \partial\hat{\psi}_r/\partial r + 2\sin(2\theta) = 0 & \text{at } r = 1 & \text{for } 0 \le \theta \le \pi/2 \\ \hat{\psi}_r = 0 & \text{at } \theta = \pi/2 & \text{for } 1 \le r < \infty \\ \hat{\psi}_r \to 0 & \text{as } r \to \infty & \text{for } 0 \le \theta \le \pi/2 \\ \hat{\psi}_r = 0 & \text{at } \theta = 0 & \text{for } 1 \le r < \infty \end{cases} \tag{3.3}$$

for external counterflow. The injection velocity Λ does not appear in the boundary conditions for $\hat{\psi}_r$ and only enters through $\hat{\psi}_p$. The numerical method used will be nearly identical for the uniform flow and counterflow. The only differences are the grid and boundary conditions, as specified above.

The domain is set up in cartesian coordinates with a cylinder of radius 1 at the origin. This means the cartesian form of (3.1) must be solved. (3.1) is first converted into the weak form so that it can be used with finite element methods. [7] This is done by multiplying (3.1) by a test function T and then integrating over the domain. By applying integration by parts to the left hand side, the order of the differential equation is reduced. The first order derivatives disappear due to the boundary conditions. Therefore, written in weak form the governing equation simplifies to

$$-\int_V \frac{\partial\hat{\psi}_r}{\partial x}\frac{\partial T}{\partial x} - \int_V \frac{\partial\hat{\psi}_r}{\partial y}\frac{\partial T}{\partial y} = -\int_V T\hat{\omega} \tag{3.4}$$

where $\int_V$ denotes integration over the computational domain.

The injection velocity Λ does not appear in the boundary conditions for $\hat{\psi}_r$; it enters only through $\hat{\psi}_p$, which may offer a simplification. The general strategy is to solve the Poisson equation for $\hat{\psi}_r$ and calculate $\partial\hat{\psi}_r/\partial r$ at $r = 1$ for $0 < \theta < \pi$ to evaluate the difference Δ between that function and $-2\sin\theta$, on that boundary, which must vanish to satisfy the first boundary condition. The assumed function $-\hat{\omega}(\theta)$ is then increased by an

amount proportional to this difference Δ, and the solution process is repeated, again and again, until the difference Δ is less than at least 10^{-2}. The iterative scheme is initialized with the known potential solution, which corresponds to $\hat{\psi}_r = 0$ and $-\omega = 0$, and the increase at each step may best be taken to be the difference Δ divided by Λ. Usually only a small number (5 or 10) of iterations is needed, but that number increases substantially as Λ decreases below 0.1.

In the indicated procedure, the constancy of the vorticity along streamlines enables the source term in the Poisson equation to be evaluated throughout the field as a function of the stream function, but the stream function is unknown. That necessitates an inner sub-iteration in which, for each Poisson-equation solution, the stream function is evaluated as a function of r and θ from the previous solution. As previously mentioned, the initial stream function used is the potential solution. This sub-iteration should be continued until subsequent solutions throughout the field change by less than two significant figures, and in this work it was continued until the change was less than 10^{-5}.

By combining the iterative methods for the vorticity distribution on the cylinder and the stream function, it is always possible to find a solution with zero tangential velocity for any $\Lambda > 0$. Stability problems were often encountered, so a number of methods were used to facilitate convergence including incorporation of a relaxation factor for the vorticity and stream function and implementation of an adaptive mesh.

Chapter 4

Selected numerical results

The problems defined above in (2.17)–(2.21) were solved numerically using the iterative scheme described in an Appendix. Results were obtained for injection conditions corresponding to values of Λ in the range $0.1 \leq \Lambda \leq 10$, with selected illustrative results presented below in Figs. 4.1–4.4.

Streamlines and accompanying vorticity distributions are shown in Fig. 4.1. Note that, in the inviscid limit $Re \gg 1$ considered here, the boundary streamline $r_s(\theta)$, marked in each plot with a thicker line, provides the approximate location of the flame (with small relative errors of order of the dimensionless mixing-layer thickness $Re^{-1/2}$). As can be seen from the evolution of the flow for increasing Λ, the outward flame displacement associated with augmented fuel injection is much more pronounced for uniform external flow, while for the counterflow the linearly increasing velocity of the external streams exerts a confining effect that precludes the flame from moving far away from the cylinder.

For the inviscid planar flow analyzed here vorticity remains constant along streamlines and is identically zero in the outer air stream. In the fuel stream, its distribution is determined by the injection process, with corresponding distributions shown by color contours in Fig. 4.1. The important effect of vorticity is illustrated by comparing the numer-

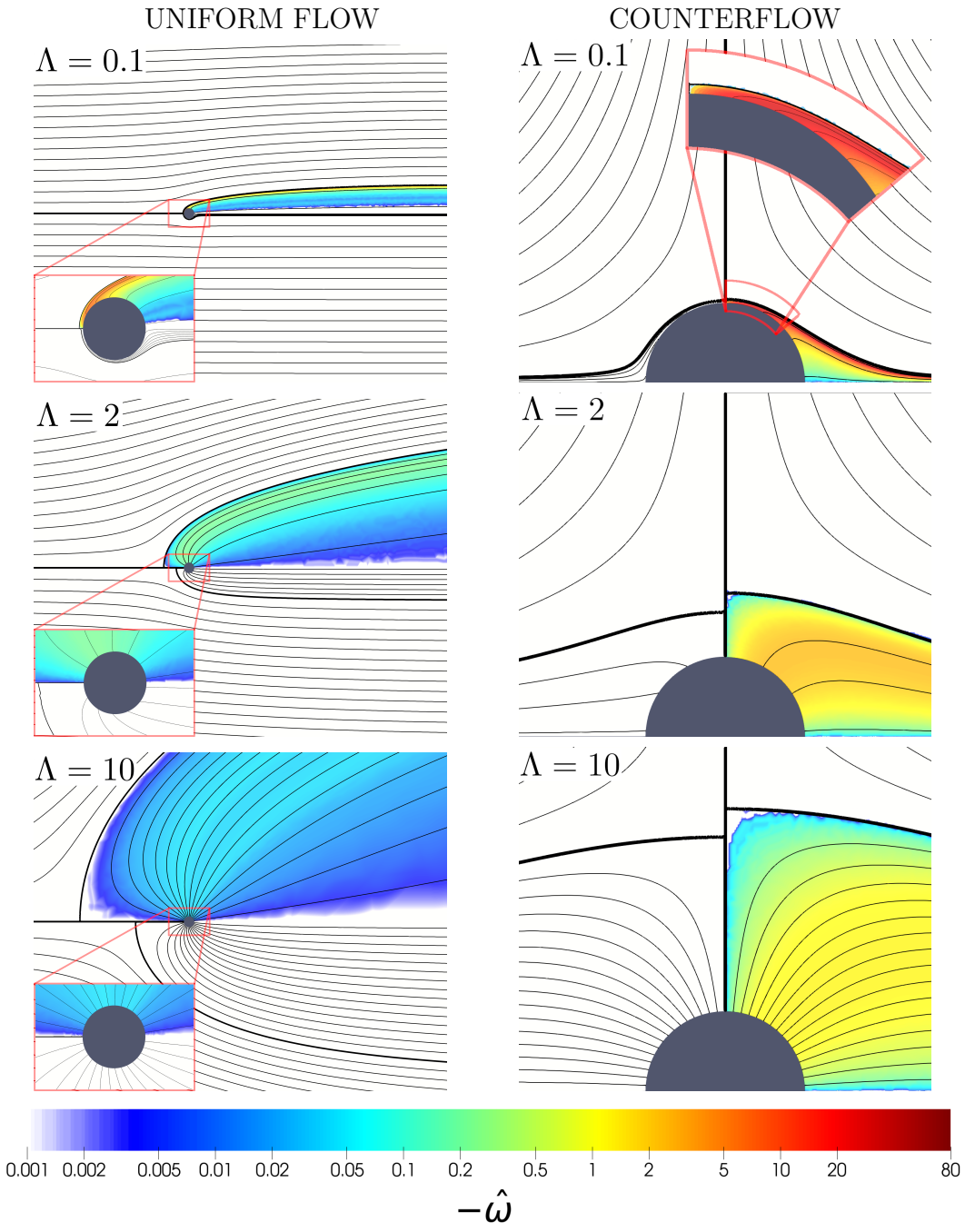

Figure 4.1: The upper half of each panel represents the streamlines and vorticity distribution corresponding to the uniform flow configuration for different values of Λ obtained by integration of (2.17) with boundary conditions (3.2) (uniform flow) or (3.3) (counterflow). The lower half shows the streamlines of the corresponding potential flow, evaluated with use made of (2.24). In the uniform-flow plots (left-hand side) the spacing used for the streamfunction is $\delta\hat{\psi} = 2$ on the air side $\hat{\psi} > 0$ and $\delta\hat{\psi} = (0.1, 1, 2)$ for $\Lambda = (0.1, 2, 10)$ on the fuel side $\hat{\psi} < 0$, except for the inset corresponding to $\Lambda = 0.1$, which uses $\delta\hat{\psi} = 0.05$. In the counterflow plots (right-hand side) the spacing used for the streamfunction is $\delta\hat{\psi} = (1, 2, 2)$ for $\Lambda = (0.1, 2, 10)$ on the air side $\hat{\psi} > 0$ and $\delta\hat{\psi} = (0.05, 1, 1)$ for $\Lambda = (0.1, 2, 10)$ on the fuel side $\hat{\psi} < 0$, except for the inset corresponding to $\Lambda = 0.1$, which uses $\delta\hat{\psi} = 0.02$.

ical results with the potential-flow solution (2.24), including the corresponding boundary streamlines

$$\begin{cases} r_s = \sqrt{1+\left[\frac{(\pi-\theta)\Lambda}{2\sin\theta}\right]^2} + \frac{(\pi-\theta)\Lambda}{2\sin\theta} & \text{(uniform flow)} \\ r_s = \left\{\sqrt{1+\left[\frac{(\pi/2-\theta)\Lambda}{\sin(2\theta)}\right]^2} + \frac{(\pi/2-\theta)\Lambda}{\sin(2\theta)}\right\}^{1/2} & \text{(counterflow)} \end{cases} . \tag{4.1}$$

The observed differences are more dramatic in cases with small injection $\Lambda \ll 1$, where the amount of vorticity needed at injection to satisfy the condition of zero tangential velocity is very large. As can be seen in the plots, for these cases with small injection velocity, the boundary streamline of the potential-flow solution tends to remain at distances of order $r_s - 1 \sim \Lambda$ from the cylinder surface. By way of contrast, when vorticity is accounted for, the boundary streamline separates from the surface. For the counterflow, separation, occurring at $\theta \simeq \pi/4$, yields to the formation of a low-velocity closed cavity. For uniform external flow the boundary streamline detaches at $\theta \simeq 3\pi/4$ and evolves downstream to produce a massive wake with vanishing fluid motion, markedly different from that encountered in the potential-flow solution.

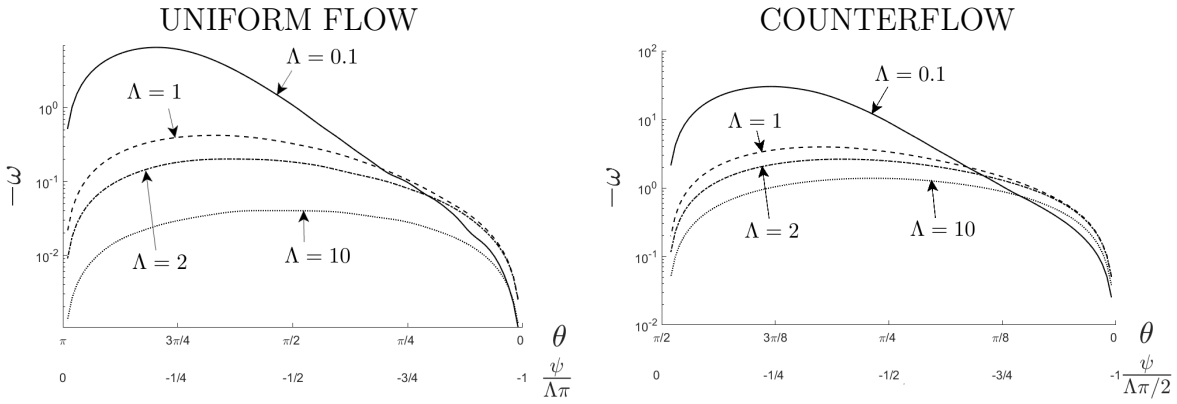

Figure 4.2: The functions $\omega(\psi) = \omega_w(\theta)$ for selected values of Λ.

A more detailed quantification of the vorticity generated in the fuel-injection process is given in Fig. 4.2. The amount of vorticity decreases for increasing injection velocities.

To understand this, one can use the potential solution (2.24) to evaluate the tangential-to-normal velocity ratio on the cylinder surface, yielding $2\sin\theta/\Lambda$ for external uniform flow and $2\sin(2\theta)/\Lambda$ for external counterflow. Since this ratio is inversely proportional to Λ, the local *spin* needed to deflect the injection velocity in the direction normal to the surface is smaller for larger Λ. Correspondingly, the vorticity generated at injection is small for large injection velocities and large for small injection velocities, that being the behavior displayed in Fig. 4.2.

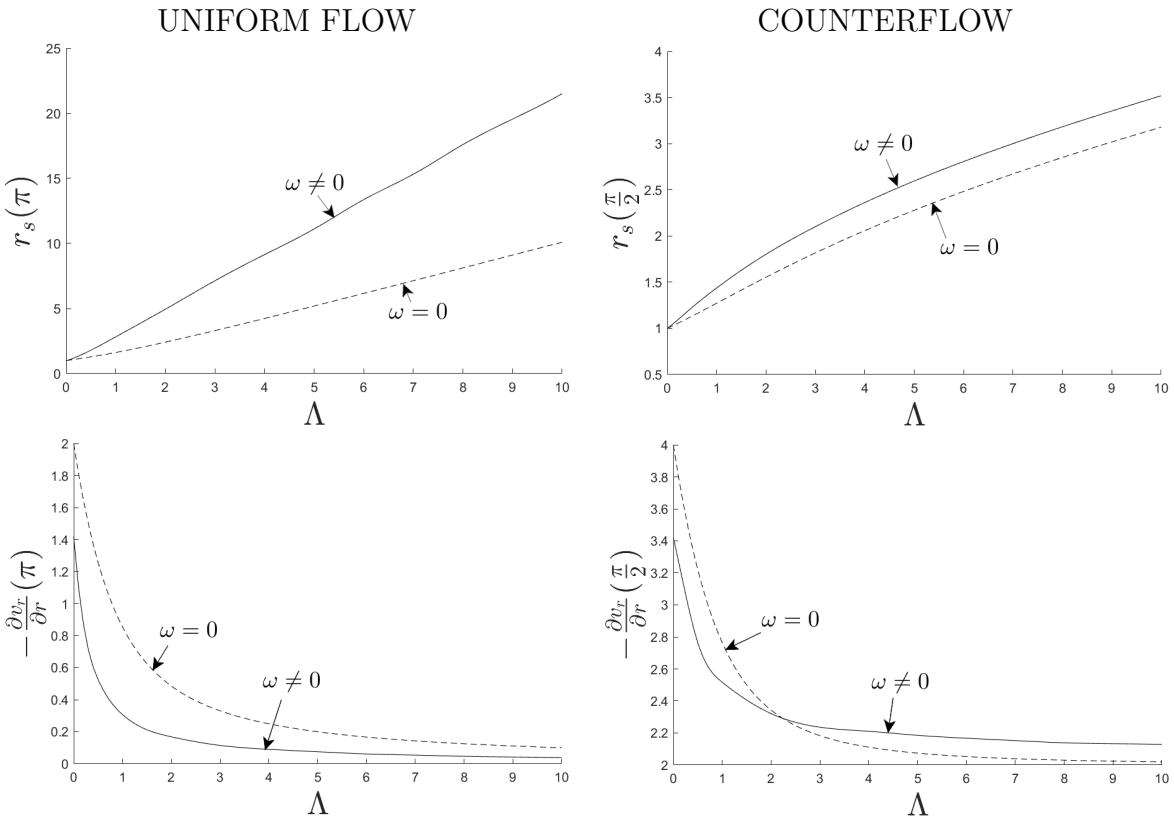

Figure 4.3: The radial location of the stagnation point and corresponding strain rate obtained by integration of (2.17) (solid curves) and from evaluation of the potential-flow streamfunction expressions (2.24) (dashed curves).

As previously mentioned, the diffusion flame sits within the mixing layer that forms about the boundary streamline $r_s(\theta)$ originating from the forward stagnation point. Since the strain rate acting on the flame can be anticipated to be largest at that point, extinction

is more likely to occur there, so that there is interest in characterizing the local flow. The results, given in Fig. 4.3, include the stagnation-point radial location $r_s(\pi)$ (uniform flow) and $r_s(\pi/2)$ (counterflow) and the associated strain rate $\hat{A}_o$, which can be evaluated from the local value of $-r_s^{-1}\partial^2\hat{\psi}/\partial r\partial\theta$. It is worth noting that the value of $\hat{A}_o$ can be used to determine the corresponding *dimensional* value of the strain rate acting on the stagnation-point flow, needed to investigate flame extinction. The values are different on the air and fuel sides, as follows from (2.16). Thus, for uniform flow the strain rate is $\hat{A}_o(U_\infty/a)$ on the air side and $\hat{A}_o(U_\infty/a)(\rho_A/\rho_F)^{1/2}$ on the fuel side, while for the counterflow the strain rate is $\hat{A}_o A_\infty$ on the air side and $\hat{A}_o A_\infty(\rho_A/\rho_F)^{1/2}$ on the fuel side.

To further assess departures from the potential solution, Fig. 4.3 displays results computed from the analytical expressions (2.24), including the stagnation-point radial location

$$\begin{cases} r_s(\pi) = \sqrt{1+(\Lambda/2)^2} + \Lambda/2 & \text{(uniform flow)} \\ r_s(\pi/2) = \left\{\sqrt{1+(\Lambda/2)^2} + \Lambda/2\right\}^{1/2} & \text{(counterflow)} \end{cases} \tag{4.2}$$

and corresponding stagnation-point strain rate

$$\begin{cases} \hat{A}_o = -\frac{1}{r}\frac{\partial^2\hat{\psi}_p}{\partial r\partial\theta} = \frac{r_s^2(\pi)+1}{r_s^3(\pi)} & \text{(uniform flow)} \\ \hat{A}_o = -\frac{1}{r}\frac{\partial^2\hat{\psi}_p}{\partial r\partial\theta} = \frac{2[r_s^4(\pi/2)+1]}{r_s^4(\pi/2)} & \text{(counterflow)} \end{cases} . \tag{4.3}$$

The comparison indicates that the potential solution describes with sufficient accuracy the location of the stagnation point and the local strain field for the case of the counterflow configuration, in agreement with the previous findings [3]. In contrast, the departures observed are significantly larger for uniform flow, for which the approximate strain-rate description provided by the potential solution is unsatisfactory for all values of Λ, with relative errors becoming larger for increasing injection velocities. For the case of small injection velocities $\Lambda \ll 1$, the strain rate computed numerically approaches a limiting value $\hat{A}_o \simeq 1.2$, markedly different from the potential flow prediction $\hat{A}_o = 2$. These order-unity

differences are consistent with the large differences in streamline patterns reported in Fig. 4.1 for uniform flow with $\Lambda = 0.1$. The result has important implications for the analysis of flames stabilized in Tsuji burners, in that the value of the strain rate exerted by the air stream on the flame near the stagnation region for small injection is $\simeq 1.2U_\infty/a$, and not the widely employed potential result $2U_\infty/a$.

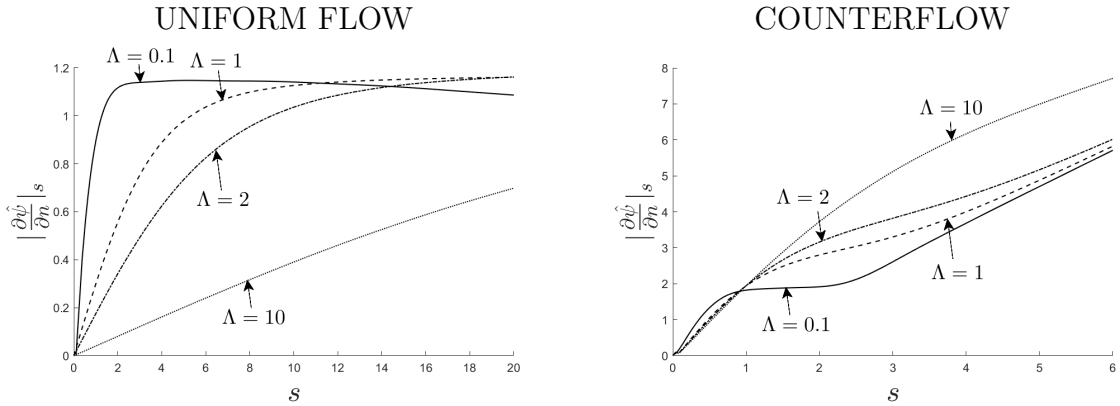

Figure 4.4: The distribution of velocity along the separating streamline $\psi = 0$ for selected values of Λ.

In the limit $Re \gg 1$, mixing and reaction in confined to the mixing layer that separates the two streams. The problem can be analyzed using as local coordinates the distance s measured along the dividing streamlines $r_s(\theta)$ and the associated transverse coordinate n, both indicated on the left-hand-side plot of Fig. 1.2. The velocities on the air and fuel side of the mixing layer satisfy (2.8). The corresponding equations for the strained mixing layer, given for instance in [8], depend on the outer flow through the local value of the strain rate, which can be computed from the streamwise variation of the velocity on the air and fuel sides of the separating streamline $\partial|\mathbf{v}^+|/\partial s$ and $\partial|\mathbf{v}^-|/\partial s$, where $|\mathbf{v}^+| = |\partial\hat{\psi}/\partial n|_s$ and $|\mathbf{v}^-| = |\partial\hat{\psi}/\partial n|_s(\rho_A/\rho_F)^{1/2}$, with $|\partial\hat{\psi}/\partial n|_s$ denoting the magnitude of the gradient of $\hat{\psi}$ at $r_s(\theta)$. The variation of $|\partial\hat{\psi}/\partial n|_s$ with s is shown for completeness in Fig. 4.4. As previously anticipated, the largest slope is found at $s = 0$, corresponding to the forward stagnation point, where the flame would be subject to the highest strain rate.

Chapter 5

Conclusions

Our numerical analysis, exploiting the limit $Re \gg 1$ while accounting for the important effects of vorticity, has unveiled a number of interesting characteristics of Tsuji burners for cases where the fuel injection is strong enough to blow the boundary layer away from the cylinder surface. A formulation has been derived that reduces the dependence of the flow to a single parameter, namely, a density-weighted injection velocity, defined in (2.22) and (2.23) for the two flow configurations considered in our paper. The analysis reveals, in particular, significant differences between the potential solution, involving a nonzero velocity component on the surface of the porous cylinder, and the solution with fuel injection normal to the cylinder surface prevailing in most applications. In the limit of small injection velocities, the analysis reveals early separation of the fuel-air interface from the vicinity of the cylinder. For the cylinder of radius a immersed in a uniform air flow with velocity U_∞, separation leads to the formation of a large wake, with the result that the potential flow solution becomes inaccurate everywhere. The results seem to indicate that the classical assumption that the strain rate for the flame near the forward stagnation point is approximately given by the potential-flow value $2U_\infty/a$ might have to be revisited. To try to further clarify this important aspect of the weak-injection limit, as well as the

structure of the flow in the opposite limit of large injection velocities, specific consideration should be given in future work to the asymptotic structure of the solution for $\Lambda \ll 1$ and $\Lambda \gg 1$.

Material from this thesis is currently being prepared for publication in Combustion Science and Technology and Combustion and Flame. This thesis is coauthored with Sánchez, Antonio; Graña, José; and Williams, Forman. The thesis author is the primary author of this material.

Bibliography

[1] H. Tsuji, I. Yamaoka, The counterflow diffusion flame in the forward stagnation region of a porous cylinder, Proc. Combust. Inst. 11 (1) (1967) 979–984.

[2] H. Tsuji, Counterflow diffusion flames, Prog. Ener. Combust. Sci. 8 (2) (1982) 93–119.

[3] M. Severino, M. Donini, F. Fachini, Diffusion flames with continuous geometrical change: from counterflow regime (Tsuji flame) to coflow regime (Burke-Schumann flame), Combust. Flame submitted (2021).

[4] J. Carpio, A. Liñán, A. L. Sánchez, F. A. Williams, Aerodynamics of axisymmetric counterflowing jets, Combust. Flame 177 (2017) 137–143.

[5] A. Weiss, W. Coenen, A. Sánchez, Aerodynamics of planar counterflowing jets, J. Fluid Mech. 821 (2017) 1–30.

[6] F. A. Williams, Combustion Theory, 2nd Edition, Addison-Wesley Publishing Co., 1985.

[7] H. Langtangen, K. Mardal, Introduction to Numerical Methods for Variational Problems, 1st Edition, Creative Commons, 2019.

[8] A. Linán, F. Williams, Ignition in an unsteady mixing layer subject to strain and variable pressure, Combust. Flame 95 (1-2) (1993) 31–46.